



Characteristics of the Heliospheric Current Sheets at the Sector Boundaries: Wind Observations from 1995–2020

Kan Liou¹ and Chin-Chun Wu²

¹ The Johns Hopkins University Applied Physics Laboratory, Laurel, MD 20723, USA; kan.liou@jhuapl.edu

² Naval Research Laboratory, Washington, DC, USA

Received 2021 July 8; accepted 2021 July 16; published 2021 October 11

Abstract

We report results of a statistical study of 1197 heliospheric current sheet (HCS) events associated with the sector boundaries observed by the Wind spacecraft between 1995 and 2020. The average property of the HCS events can be characterized as follows: (1) The width of the current sheets ranges between ~ 600 km and 1.1×10^6 km, with an average width of $1.06 \pm 2.37 \times 10^5$ km; (2) The longitude (in Geocentric Solar-Ecliptic coordinate) of the HCS normal shows a large peak at $\sim 210^\circ$ (0° sunward pointing) and a longer tail at smaller angles; (3) The latitudinal angle (inclination) of the HCS normal shows a near symmetric distribution (peak and average $\sim 0^\circ$); (4) The yearly occurrence rate is relatively constant (~ 46 or 3.4 events per solar rotation), without showing a clear solar cycle dependence; (5) There are solar cycle variations in the properties of the plasma and field within the current sheets and these variations follow closely with the background solar wind plasma and field; (6) A mild ($\sim 10\%$) proton temperature increase within the HCS, suggesting that heating of the solar wind proton can occur within the current sheet; and (7) A sudden decrease in the proton temperature anisotropy (T_{\parallel}/T_{\perp}) toward unity within ~ 3 hr of the HCS was identified. These results suggest that on the large scale the HCS at 1 au is a relatively stable and persistent solar wind structure throughout the solar cycle. On the small scale the HCS property is probably controlled by the dynamics of the current system, which is still poorly known.

Unified Astronomy Thesaurus concepts: [Heliosphere \(711\)](#)

1. Introduction

The interplanetary magnetic field (IMF) is structured into sectors of either inward or outward polarity separated by relatively sharp boundaries, known as the sector boundary (SB), lasting from a few minutes to a few hours (Ness & Wilcox 1964; Wilcox & Ness 1965). Early studies of the SB led to the discovery of the heliospheric current sheet (HCS; see, e.g., Smith 2001 for a detailed review). The HCS is loosely defined as a thin layer of plasma that divides two oppositely directed global heliospheric magnetic fields originating from the Sun. It is surrounded by a region of plasma characterized by proton density and depressed magnetic field called the heliospheric plasma sheet (HPS; Winterhalter et al. 1994). The direct measurement of the HCS by spacecraft in the heliosphere is a large ($>120^\circ$) directional discontinuity in the IMF. Alternatively, a 180° rotation in the pitch angle of super-thermal ($>\sim 80$ eV) electron strahls has also been shown to be a good indicator of sector crossings (Kahler & Lin 1994, 1995). When this method is employed, the SB is also called the true sector boundary (e.g., Crooker et al. 2004). While most of the HCS is found to be accompanied by an SB, there are cases where they do not coincide (Owens & Forsyth 2013; Liu et al. 2014). Nonetheless, the terms HCS and SB will be considered the same phenomenon and will be used interchangeably without losing generality.

The HCS is believed to be generated at the cusp of the streamer belt and is the interplanetary extension of the solar neutral line (e.g., Schulz 1973; Hundhausen 1977). The HCS is known to be the largest and persistent solar wind structure in

the heliosphere. It has been observed near the Sun as close as 0.165 au by Parker Solar Probe (Lavraud et al. 2020; Szabo et al. 2020) and near the termination shock (~ 94 au) by Voyager-1 (Richardson et al. 2006; Burlaga et al. 2007). Early studies of the HCS focused on its large-scale configuration. The most intriguing feature of the HCS is its warped shape resembling a *ballerina skirt* (Wilcox et al. 1980). Ideally, the Sun's dipole field prevails and the HCS would lie in the elliptic plane of slow solar wind with fast solar wind at higher latitudes in both hemispheres. Due to an offset of the solar dipole axis from the Sun's rotational axis, the HCS becomes warped after stretching out of the Sun by the solar wind (e.g., Pizzo 1991). When the spacecraft orbital plane cuts through the warped HCS, it results in alternating magnetic sectors of opposite polarities. The warped current sheet surface varies with the phase of the solar cycle. Using source surface map and the potential field model Hoeksema et al. (1983) calculated that near the solar minimum, the latitudinal extent of the HCS is limited within 15° , whereas the extent can be greater than 50° during solar maximum conditions. While it is suggested that the inclination of the HCS at 1 au can be reliably predicted by the source surface model when transient events such as interplanetary (IP) shocks or bidirectional electrons are absent (Burton et al. 1994), observations of such a solar cycle variation have not been established.

The HCS is embedded within the slow solar wind and a region of elevated proton density and proton beta (Winterhalter et al. 1994). Statistical studies using superposed epoch analysis suggest that the HCS is grossly characterized by a local maximum in the proton density and a local minimum in proton temperature and speed (e.g., Borrini et al. 1981; Suess et al. 2009). These gross properties can be reproduced by a three-dimensional magnetohydrodynamic (MHD) model with a *tilted dipole* (Pizzo 1991).



Original content from this work may be used under the terms of the [Creative Commons Attribution 4.0 licence](#). Any further distribution of this work must maintain attribution to the author(s) and the title of the work, journal citation and DOI.

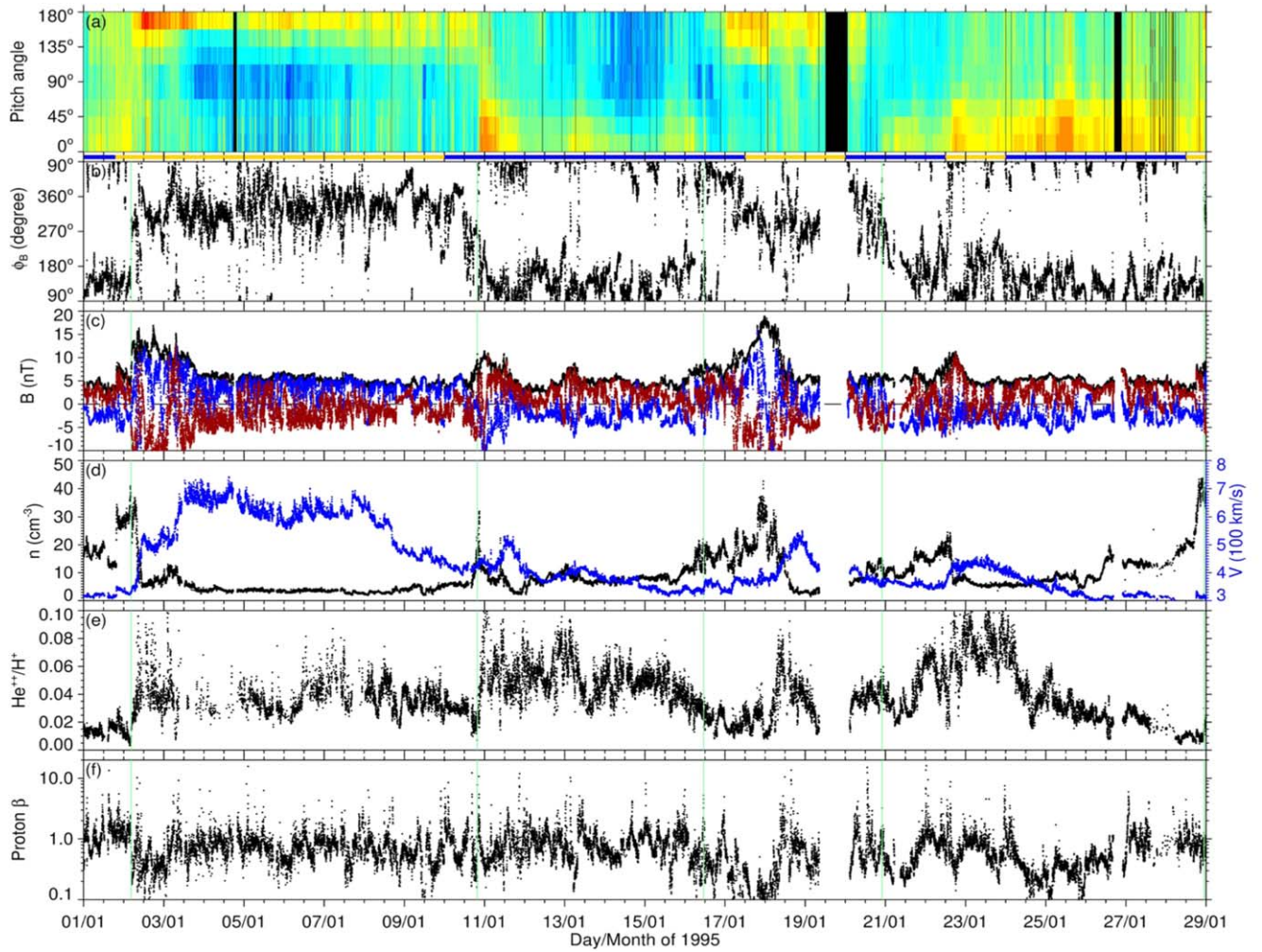


Figure 1. Wind measurements of (a) super-thermal electron (~ 375 eV) pitch angles, (b) magnetic field azimuthal angles, (c) magnetic field x -component (blue), y -component (red), and intensity (black), (d) proton density (black) and bulk speed (blue), (e) alpha-to-proton density ratio, and (f) proton beta on 1995 January 1–28. The green vertical lines indicate HCS crossings.

The local structure of the HCS is generally complex. Part of this can be realized by the large variability in the HCS width. For example, previous observations suggested that the width of the HCS at 1 au varies significantly, ranging statistically from ~ 0.35 to 1.2×10^4 km (95% confidence intervals) (Winterhalter et al. 1994) to 6×10^4 km (average) (Lepping et al. 1996). Much wider ones, on the order of $\sim 10^6$ km, have also been reported lately (Blanco et al. 2008). There is evidence that the width of the HCS shrinks with the radial distance (Zhou et al. 2005). It is still not known what controls the width of the HCS, especially if such a wide range of thickness depends on the solar cycle. Recent studies have shown that there is a solar cycle effect on the width of the HPS (Wu et al. 2019) and the width of the slow wind region (SWR; Liou & Wu 2016). They proposed an HPS inflation hypothesis in which the HPS is wider when the latitudinal magnetic pressure gradient is smaller and becomes narrower when the pressure gradient is larger (e.g., Wu et al. 2016). Because both the SWR and the HPS encase the HCS, there is a possibility that the width of the HCS is also controlled by the solar cycle.

Previous theoretical and observational studies have contributed to our current knowledge of the HCS. However, the majority of these works are associated with case studies. Until now, there has been no true long-term (entire solar cycle or

longer) statistical study of the HCS. There is a question about how general the above-mentioned HCS knowledge can be applied. The purpose of this study is to conduct a detailed analysis of a large number of the HCS events that span over a solar magnetic cycle (the Hale cycle) to establish the characteristics of the HCS at 1 au.

2. Survey of HCS Events

We survey the solar wind plasma and magnetic field data acquired by the Solar Wind Experiment (SWE; Ogilvie et al. 1995) and Magnetic Field Instrument (MFI; Lepping et al. 1995) on board the Wind spacecraft from 1995–2020 to search for HCS crossings. In addition, super-thermal electron data acquired by the 3D Plasma Instrument (3DP; Lin et al. 1995) are used to make sure the current sheet event is associated with the SB. Figure 1 shows an example of the identified HCS events for the first 28 days of Wind measurements in 1995. There are five candidate HCS crossings: January 2, 10, 16, 20, and 28. As shown in Figures 1(a) and (b), these events are associated with an $\sim 180^\circ$ change in the super-thermal electron pitch angles and the magnetic field azimuthal angles. For example, the first event is associated with a change in the IMF from a toward to an away sector. The super-thermal electron

pitch angle changed from parallel to antiparallel. This can also be clearly identified in the IMF data in Figure 1(c). After January 10, the IMF changed from an away sector (away from the Sun) to a toward sector (toward the Sun) and the super-thermal electron pitch angle changed from antiparallel to parallel. A similar feature is also evident for the rest of the events. These HCS crossings coincided with a local density maximum and solar wind speed minimum (see Figure 1(d)), a local minimum in the alpha-to-proton density ratio (Figure 1(e)), and a local maximum in the proton beta (β : ratio of proton thermal pressure to magnetic pressure). These are typical characteristics of the solar wind near the HCS (e.g., Borini et al. 1981; Winterhalter et al. 1994) and are used to help determine HCS crossing events.

A total of 1197 candidate HCS crossing events are identified with the Wind data from 1995–2020. This translates to ~ 46 events per year or ~ 3.4 events per solar rotation. Note that multiple current sheet crossings can occur within a day. In this case, we selected the first one as our candidate HCS event. Furthermore, given the fact that there are data gaps ($\sim 8\%$) in Wind data, especially in 1999–2004 when the Wind spacecraft was in Earth’s magnetosphere, the actual occurrence rate could be proportionately higher.

2.1. HCS Structural Analysis

After the candidate events are identified, the precise HCS crossing times are determined by detailed analysis of the candidate HCS using the method developed by Blanco et al. (2003). This method fits the magnetic field data around the current sheet by a rotated one-dimensional Harris current sheet (Harris 1962). Assuming a planar current sheet in the x - z plane in the Geocentric Solar-Ecliptic (GSE) coordinate system, the three components of the magnetic field (\mathbf{B}) around the Harris current sheet can be expressed by $\mathbf{B} = [B_0 \tanh((y - y_0)/L) + B_{0x}, B_{0y}, B_{0z}]$, where B_{0x} , B_{0y} , and B_{0z} are the three components of the magnetic field immediately outside the current sheet, y_0 is the center location of the HCS, and L is the half-width of the current sheet. After two consecutive rotations (first around the z -axis by α degrees and the around the x -axis by β degrees), the three components of the Harris current sheet field can be expressed by

$$B_x = \left[B_{0x} + B_0 \tanh\left(\frac{y - y_0}{L}\right) \right] \cos(\alpha) + B_{0y} \sin(\beta), \quad (1)$$

$$B_y = \left[B_{0x} + B_0 \tanh\left(\frac{y - y_0}{L}\right) \right] \sin(\alpha) \cos(\beta) + B_{0y} \cos(\alpha) \cos(\beta) - B_{0z} \sin(\beta), \quad (2)$$

$$B_z = \left[B_{0x} + B_0 \tanh\left(\frac{y - y_0}{L}\right) \right] \sin(\alpha) \sin(\beta) + B_{0y} \cos(\alpha) \sin(\beta) - B_{0z} \cos(\beta). \quad (3)$$

To apply Equations (1)–(3) to time series data, the y and y_0 coordinates and the current sheet half-width L can be converted to time through the following relations: $y = (\mathbf{n} \cdot \mathbf{v})t$, $y_0 = (\mathbf{n} \cdot \mathbf{v})t_0$, and $L = (\mathbf{n} \cdot \mathbf{v})\tau$, where \mathbf{v} is the solar wind velocity (assuming the spacecraft velocity can be ignored), τ is the half-width of the crossing time, and $\mathbf{n} = [-\sin(\alpha), \cos(\alpha) \cos(\beta), \cos(\alpha) \sin(\beta)]$ is the normal direction of the current sheet. Therefore, the term in the parenthesis of the hyperbolic tangent becomes $(t - t_0)/\tau$. To fit Equations (1)–(3) to the measured magnetic field around the candidate HCS, we apply the Levenberg–Marquardt least-squares fit, which minimizes the sum of squares of the deviations with

seven unknown parameters (B_0 , B_{0x} , B_{0y} , B_{0z} , α , β , t_0 , and τ). This is done with 3 s magnetic field data to increase the statistics. Once a fit is obtained, we can calculate the normal orientation (\mathbf{n}) and width ($2L$) of the current sheet.

The results of the HCS analysis are summarized in Figure 2 and Table 1. Figure 2(a) shows a histogram of the HCS numbers in terms of the magnetic field rotation angles (defined in the GSE x - y plane). While the majority ($\sim 71\%$) of the HCS events are associated with large ($>120^\circ$) field rotation, some non-negligible ($\sim 29\%$) number of events are associated with a small ($<120^\circ$) field rotation. The average value is 137° (with a standard deviation of 33°) and the median value is 142° . The width of the HCS (see Figure 2(b)) ranges between ~ 600 and 1.1×10^6 km, with an average width of 1.06×10^5 km, a median of 5.9×10^4 km, and a large standard deviation (σ) of 2.37×10^5 km. These numbers generally fall within some previously reported results (e.g., Winterhalter et al. 1994; Lepping et al. 1996; Blanco et al. 2008). The large standard deviation indicates the wide spread of the HCS width as shown in Figure 2(b). The histogram shows a linear relationship between the logarithmic of event numbers and the current sheet width and the relation, from the least-squares fit, can be expressed as $\ln(N) = 4.91(\pm 0.75) - 0.09(\pm 0.02)w$, where N is the HCS occurrence and w in units of 10^4 km.

While the HCS is generally considered as the heliospheric extension of the solar magnetic equator, it does not lie in the equatorial plane but is twisted northward and southward (e.g., Smith 1993). As a result, a tilted HCS should be commonly observed by a spacecraft traversing the HCS. Figure 2(c) shows a histogram of the latitudinal angles of the HCS normal direction in GSE coordinates. A small absolute angle indicates a large tilt, whereas a large absolute angle indicates a small tilt of the current sheet. While the latitudinal angle of the HCS is widely spread within the maximum $\pm 90^\circ$ range, the event distribution is roughly symmetric about small angles, with an average value of 0° ($\sigma \sim 43^\circ$), a median value of -2° , and a significant peak around -15° . The majority ($\sim 2/3$) of the latitude is confined within $\pm 45^\circ$ of the ecliptic plane, indicating a large inclination for the majority of the HCS at 1 au.

Figure 2(d) shows a histogram of the longitude of the HCS normal direction in GSE coordinates. The longitudinal angle ranges between 90° and 270° , with a large peak at $\sim 210^\circ$ and with a longer tail at smaller angles ($\sim 135^\circ$). This suggests that the majority of the HCS events at 1 au lie in the 120° – 300° plane and the minority of events lie in the 45° – 225° plane. These two plane are close to the nominal longitude of the Parker spiral field near Earth in GSE coordinates (e.g., $\sim 135^\circ$ for the away and $\sim 315^\circ$ for the toward IMF). We suspect that the HCS lies along the true background field. To test our hypothesis, we analyze hourly averages of the magnetic field azimuthal angles at the HCS events and the results are shown in Figure 3. It can be clearly seen that the majority of the fields are clustered around two angles, one at $\sim 130^\circ$ (toward) and the other at $\sim 300^\circ$ (away). These angles are not too far from the typical orientation for the Parker spiral field at 1 au. Figure 3(b) shows a histogram of the angle difference between the HCS orientation and the ambient field orientation. Although there is a wide spread of the difference, the majority of the HCS events lie within $\pm 24^\circ$ ($\sigma = 48^\circ$) from their ambient field.

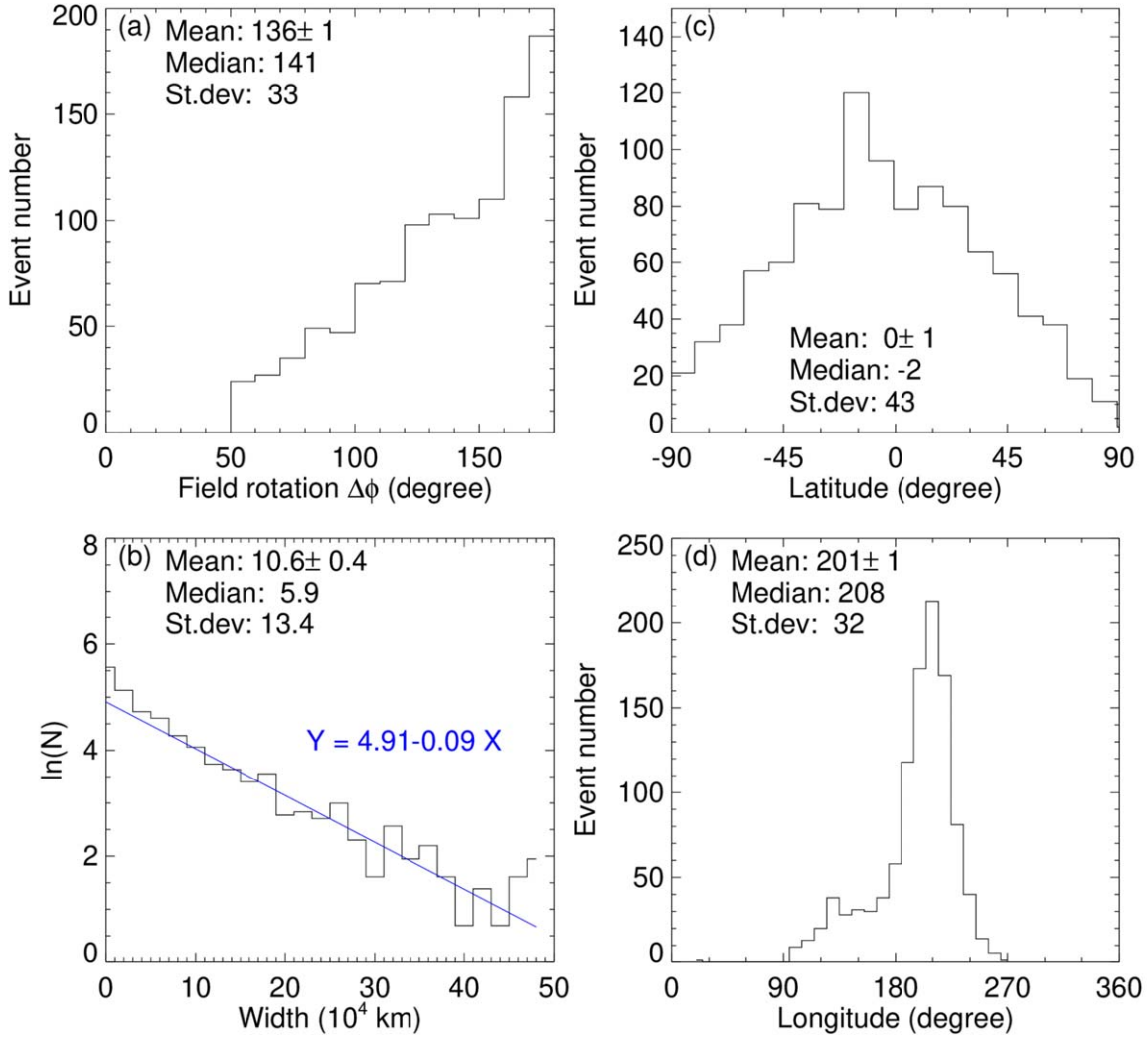


Figure 2. Histogram of (a) the rotation angle across and measured in the HCS, (b) the width of the HCS, (c) the longitudinal angle of the HCS normal, and (d) the latitudinal angle of the HCS normal. The straight blue line in panel (b) is the least-squares linear fit of the histogram data. The mean, median, and standard deviation values are inserted in each panel.

Table 1

Summary of the Average Geometry of the HCS from 1197 HCS Events

HCS Parameters ($N = 1197$)	Mean	Standard Deviation (σ)	Median
Rotation Angle $\Delta\phi$ (degree)	$136^\circ(\pm 1^\circ)$	33°	141°
Width (km)	$1.06(\pm 0.04) \times 10^5$	1.34×10^5	5.9×10^4
Longitude (degree)	$201^\circ(\pm 1^\circ)$	32°	208°
Latitude (degree)	$0^\circ(\pm 1^\circ)$	43°	-2°

2.2. Solar Cycle Variations

It is generally perceived that the configuration of the HCS varies with the 11 yr solar cycle (see Smith 2001 for a detailed review). This is supported by extrapolation of the neutral sheet in the photosphere using the potential field model (Hoeksema et al. 1983) and numerical MHD simulations (e.g., Riley et al. 2002). During the solar minimum years the HCS is confined to

the low-latitude region, whereas during the solar maximum years it becomes tilted and extends to higher latitudes. Therefore, it is expected that there is a better chance for a spacecraft to encounter the HCS during the solar maximum years than for the solar minimum years. Here we investigate this possibility by arranging the identified HCS events and their properties by year and the results are summarized in Figure 4. Figure 4(a) shows the yearly occurrence of the HCS events, along with the yearly sunspot number (SSN). As mentioned in the previous section, there are solar wind data gaps between 1999 and 2002. We normalize the yearly event numbers by assuming an equal occurrence rate and the result is shown in Figure 4(a) as red dots. Surprisingly, there is no clear solar cycle variation (correlation coefficient $r = 0.18$). We also check if there is a difference between odd and even solar cycles. Surprisingly, there is no significant difference between solar cycle 23 (581 in total from 1996–2007) and solar cycle 24 (593 in total from 2008–2019) either.

Figures 4(b)–(d) show the yearly width, longitude, and latitude of the HCS. The yearly averages of the HCS width vary significantly, ranging between $\sim 4 \times 10^4$ and 1.2×10^5 km. There is no clear variation associated with the SSN. The yearly average longitudes of the normal of the HCS are relatively stable and

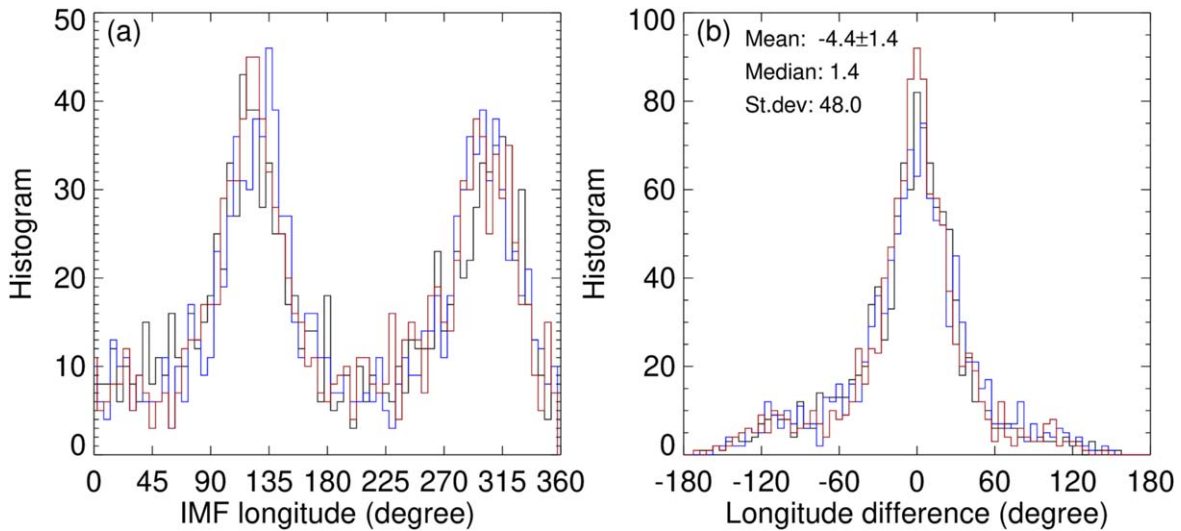


Figure 3. (a) Histogram of the longitudinal angle of the hourly average of the IMF surrounding the HCS; (b) histogram of the difference (in degree) between the IMF longitude and the HCS longitude. The mean, median, and standard deviation values are inserted in panel (b). In both panels, the blue and red traces represent values derived from the hourly solar wind data 1 hr before and after the current sheet.

cluster around $\sim 200^\circ$ (measured from the GSE x -axis). If the HCS are aligned with the IMF spiral field, this result is consistent with the finding that the averaged IMF spiral angles are statistically fixed and show little dependence on the phase of the solar cycle (Borovsky 2010). The yearly averages of the normal of the HCS latitude fluctuates about $\pm 15^\circ$. There is no noticeable solar cycle variations either.

In addition to the configuration of the HCS, knowledge about the solar wind properties of the HCS and their solar cycle variations is also important to fully understand the current sheet evolution. Figures 4(e)–(h) show the x -component (in GSE) of the proton speed (v_x), density, thermal speed (v_{th}), and magnetic field intensity ($|B|$) within the current sheets. All parameters show similar variations over the two solar cycles (two peaks and three dips) and correlate modestly with SSN. The peak correlation coefficient is shown in the second column of Table 2. The maximum value of these solar wind parameters occurs roughly during the decline phase and the dip of these solar wind parameters occurs roughly during the solar minimum years.

To determine if the solar cycle variations of these parameters are due to solar cycle variations of the background solar wind, we also plot the yearly average solar wind parameters in Figures 4(e)–(h) as blue traces to make a comparison. Except the magnetic field intensity, which shows a good correlation with SSN ($r = 0.84$), other solar wind parameters show weak (proton density) to moderate (solar wind speed and thermal speed) correlation. This indicates that, except the proton density, the properties of HCS change with the solar wind. In terms of the magnitude of the solar wind parameters within the HCS relative to the background solar wind, the proton density within the HCS is significantly larger than the background value. The difference is more significant (a factor of ~ 5) during the decline phase and is least significant (a factor of $< \sim 2$) during the solar minimum years. For proton speed and proton thermal speed, their values are smaller than their corresponding background values, irrespective of the phase of the solar cycle. The magnitude of the magnetic field in the HCS follows closely the background magnetic field. As expected, these results

suggest that the solar wind proton density, speed, and temperature are good indicators of the HCS.

2.3. Solar Wind Gross Properties around the HCS

The solar wind properties surrounding the HCS are important indicators that provide information about the conditions where and when the HCS normally may occur. This subject has been studied in the past by some researchers using superposed analysis using limited data (e.g., Borriani et al. 1981; Winterhalter et al. 1994; Suess et al. 2009). Here we apply 26 yr of Wind data to conduct their studies with a focus on basic solar wind parameters. Figure 5 shows an overview of the superposed epoch analysis results, which from panels (a)–(h) include the solar wind density, speed, temperature, magnetic field intensity, dynamic pressure, total pressure, proton beta, and parallel-to-perpendicular (relative to the magnetic field vector) temperature ratio 6 days before and after the HCS crossings. We use 60 minute bin widths to smooth out small structures. The results are shown in Figure 5 in black traces. To explore a possible solar cycle variation, we also separate data to represent the solar minimum years (1995–1997, 2007–2009, and 2019–2020) and the solar maximum years (2000–2002, 2010, 2013–2015) and the results are plotted as blue and red traces for the solar minimum and solar maximum years, respectively.

Figures 5(a)–(d) show the solar wind proton density, speed, temperature, and magnetic field intensity and indicate that the HCS resides inside of a wider (± 1 day or more) region of elevated plasma density and magnetic field and depressed proton speed and temperature. More precisely, the current sheet is statistically located *near* the ridge of the proton density and magnetic field intensity and the valley of the proton speed and temperature. The gross characteristic features of the plasma and field in the vicinity of the current sheets mimic the gross characteristic features of stream interfaces first reported by Gosling et al. (1978) and many recent others (e.g., Yin et al. 2019). The stream interface, also known as the corotating interaction region (CIR; e.g., Smith & Wolfe 1976; Gosling & Pizzo 1999; Lee 2000), is a plasma compression region where hot and tenuous fast solar wind originating from the coronal hole overtakes the cold and dense slow wind. In addition, the

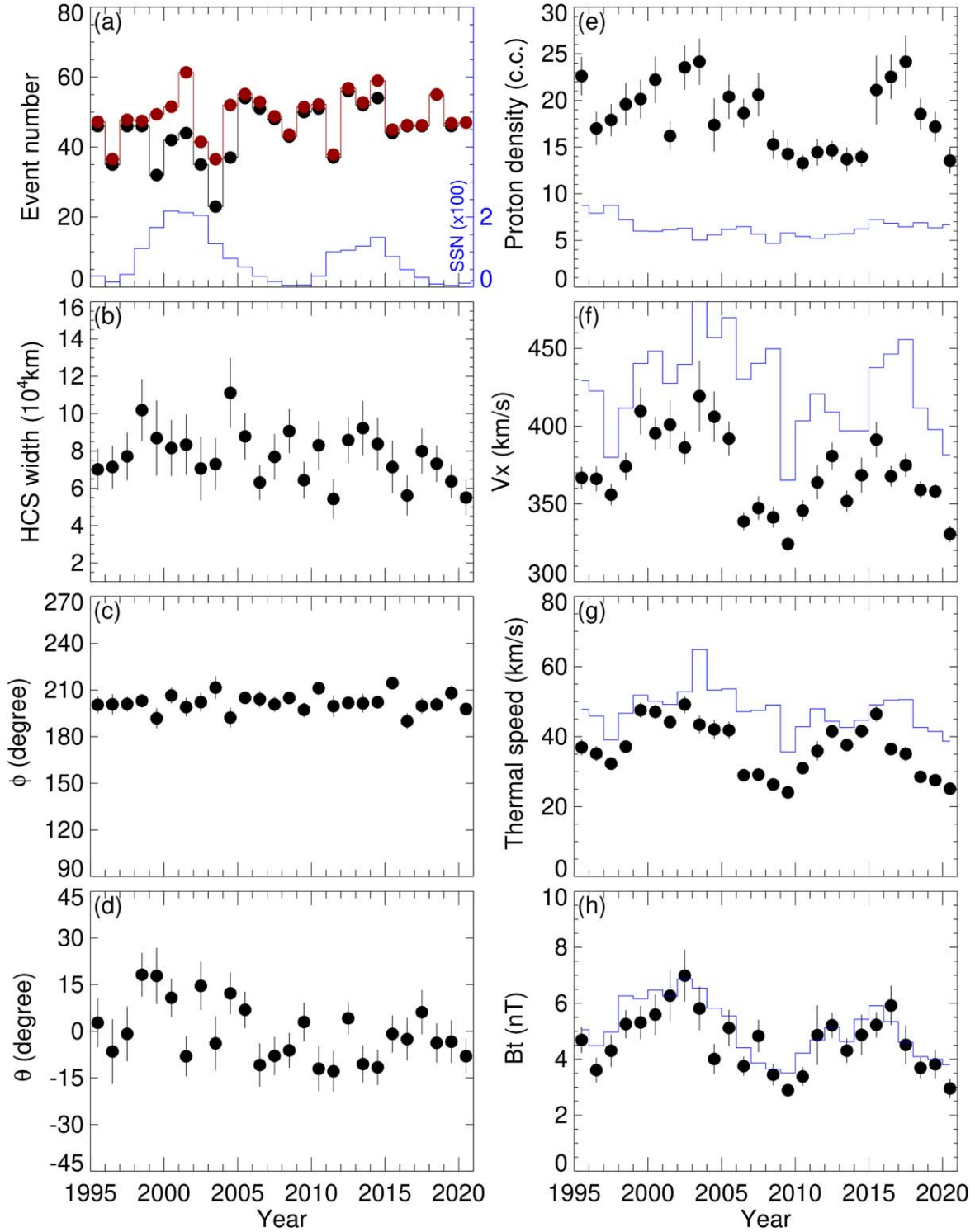


Figure 4. Panels show (a) the yearly number of the HCS events, (b) yearly averages of the HCS width, (c) the longitudinal and (d) latitudinal angles of the HCS normal, yearly averages of (e) the proton density, (f) proton velocity (x-component in GSE coordinates), (g) proton thermal speed, and (h) the magnetic field intensity. The yearly sunspot numbers are plotted in (a) as the blue traces. The red dots in (a) indicate the normalized HCS event number. The error bars indicate the standard deviation of the mean values.

slow wind ahead of the CIR is deflected westward and the fast wind behind the CIR is deflected eastward due to the pressure gradient (e.g., Siscoe 1972). Figure 5(b) also shows the y-component (in GSE) of the flow speed (the green trace). Indeed, enhanced westward flow starts a couple of days before the HCS and reduced westward flow starts after the HCS. Since

the azimuthal flow reversal is a strong indicator of the CIR, this result suggests that a large number of the HCS events are followed by a CIR. Note that while these features have also been reported previously (e.g., Borrini et al. 1981; Winterhalter et al. 1994), they are statistical properties and do not always occur at the same time in single events.

Table 2Correlation Coefficient (r) Table for the Yearly Average Plasma and Field Parameters between the Solar Wind (Row) and the HCS (Column)

$r(N = 26)$	SSN ^a	Density	Speed	Thermal Speed	$ B $
SSN	1	-0.21	0.63	0.68	0.84
Density	0.51	0.33
SW speed	0.77	...	0.68
Thermal speed	0.85	0.64	...
$ B $	0.78	0.85

Note.^a Yearly SSN.

Similar to the proton density, the proton dynamic pressure peaks at the HCS (see Figure 5(e)). While the solar wind is weaker within the current sheet, proton density (increase) dominates the dynamics of the HCS and the enhanced plasma surrounding it (e.g., the plasma sheet). The location of the HCS is very close to the total pressure (sum of the thermal pressure nkT and magnetic pressure $B^2/8\pi$) maximum (see Figure 5(f)). Note that the total pressure is more steep upstream than downstream, indicating that the structure is not stable and expanding outward.

Figure 5(g) shows the superposed proton beta (ratio of proton thermal pressure-to-magnetic field pressure). Although there are large fluctuations in the proton beta, a narrow peak can be easily seen at the HCS. An enhancement of proton beta at the HCS and its adjacent plasma has been reported and is attributed to a local depression of the magnetic field and a simultaneous enhancement in proton density (e.g., Winterhalter et al. 1994).

Temperature anisotropies are one of the important non-thermal features of the solar wind (e.g., Hundhausen et al. 1970; Feldman et al. 1973; Marsch et al. 1982a, 1982b). Here we explore proton temperature anisotropies at and adjacent to the HCS, and the result is shown in Figure 5(h), which shows the ratio of parallel-to-perpendicular proton temperature. In general, the temperature ratio is greater than unity, ranging between ~ 1.1 and 1.4 over the ± 6 days interval around the HCS. The current sheet is located at the region of the declining temperature ratio. Surprisingly, a sharp decrease in the temperature ratio from ~ 1.2 to ~ 1.1 is found at the HCS. Because of the long epoch time window (± 6 days) and the large time bins (1 hr) used in Figure 5, it is not adequate to study the finer ($\sim 10^5$ km or a few minutes in crossing time) timescale properties of the plasma around the current sheet and the current sheet itself. We will show and discuss the fine structure of the current sheet later (Section 2.4).

These features of the large-scale morphology of the HCS seem to be independent of the phase of solar cycle. This is demonstrated as the blue (solar minimum) and red (solar maximum) traces in Figure 5. Although the differences are noticeable, the general morphology of the trend around the HCS are similar. The smaller proton density and larger solar wind speed, magnetic field intensity, temperature, and total pressure under solar maximum than under solar minimum

conditions are consistent with the general solar cycle variations of the solar wind. The dynamics pressure does not change between the two conditions (Figure 5(e)), as the result of anti-correlation between the proton density and speed. The larger proton total pressure and smaller proton during solar maximum conditions than during solar minimum condition are due mainly to the larger magnetic field intensity (Figures 5(f) and (g)). Finally, proton temperature anisotropy is larger $\sim \frac{1}{2}$ day before and after the HCS in solar maximum years than in solar minimum years. There is no significant solar cycle difference $\sim \frac{1}{2}$ day around the HCS.

2.4. Solar Wind Fine Structure around the HCS

Now we return to the study of the small-scale solar wind properties around the current sheet. Figure 6 shows the key solar wind parameters around the HCS in a smaller time window (± 3 hr). Since the average current sheet width is $\sim 10^5$ km and the solar wind speed is ~ 360 km s⁻¹, it takes ~ 5 minutes to cross the HCS. Therefore, we also reduce the bin size to 2 minutes to show the structure of the current sheet. In this time window variations of plasma parameters across the current sheets are clearly visible (Figure 6(a)). The proton density indeed peaks at the current sheet, with a slightly larger density before than after the current sheets. The proton speed is relatively unchanged (~ 360 km s⁻¹). Figure 6(b) also shows that the HCS coincides with the abrupt increase in the y -component of the solar wind proton velocity from its minimum. This abrupt eastward flow reduction is not understood. We suspect that this is due to a pressure enhancement in the current sheet. This will be left for our future study when we analyze electron moment data. These are consistent with the gross plasma features around the CIR. Also, at the current sheet, an eastward excursion of the azimuthal flow occurs, followed by the flow reversal. This is consistent with the conclusion of Gosling et al. (1978) that sector boundaries lie ahead of the stream interface. We estimate the leading time being ~ 5 hr, which is consistent with the 1.5 hr–1.5 days reported by Gosling et al. (1978) based on 17 events. The separation of the HCS and stream interface (SI) generally decrease with the heliocentric distance increase (Schwenn 1990). However, coincidence of the HCS and SI events at 1 au has been reported (Huang et al. 2016), but is probably rare.

As expected, the depression of magnetic field intensity, a key feature of the current sheet, can be clearly seen in Figure 6(c). In this time interval a narrow (~ 1 hr) but large ($\Delta B/B > \sim 0.2$) dip in the magnetic field intensity associated with the current sheet is clearly shown. The width of the magnetic field depression is estimated to be ~ 1 hr (or $\sim 1.3 \times 10^6$ km for a typical solar wind speed at the HCS: 360 km s⁻¹), which is ~ 10 times wider than the average width of the current sheet. This is because sometimes multiple current sheets (magnetic depressions) are found to be close to the sector boundary, presumably associated with reconnection (e.g., Gosling 2007). In such a case the main current sheet was selected as the HCS and the rest of the minor ones are ignored. The depression of the magnetic field and the enhancement in the proton density result in an enhancement of the proton beta centered at the HCS (Figure 6(d)).

In addition, Figures 6(a)–(d) show the solar wind parameters surrounding the HCS for the solar minimum (blue traces) and solar maximum (red traces) years. Although differences in the background plasma between solar maximum and minimum are

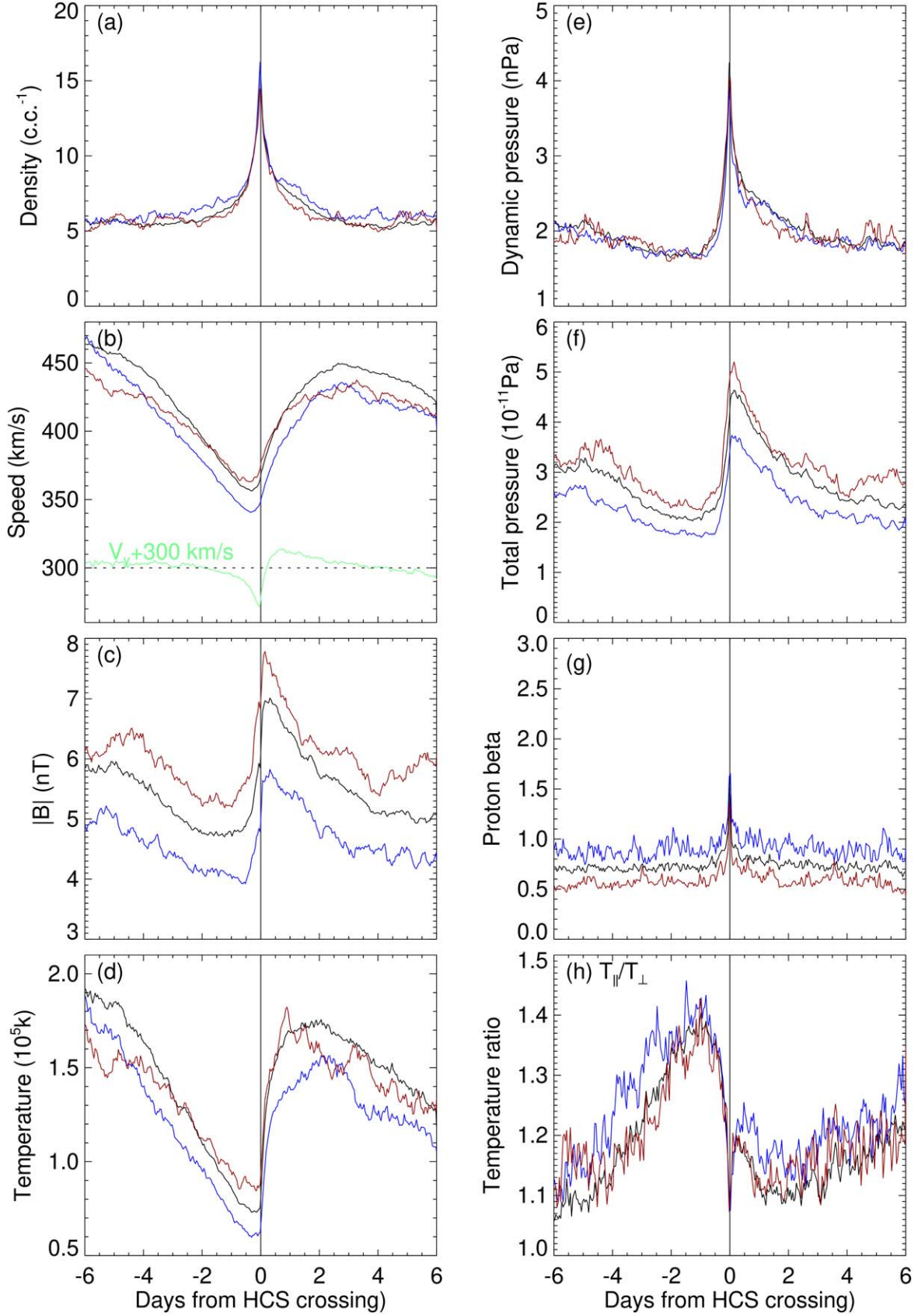


Figure 5. Superposed epoch analysis of the hourly averaged solar wind properties 6 days before and 6 days after the HCS. The panels show (a) the proton density, (b) proton speed, (c) magnetic field intensity, (d) proton temperature, (e) proton dynamic pressure, (f) total (sum of thermal and magnetic) pressure, (g) proton beta, and (h) proton parallel-to-perpendicular temperature ratio. The blue (red) traces are based on solar minimum (maximum) years data (see the text for details).

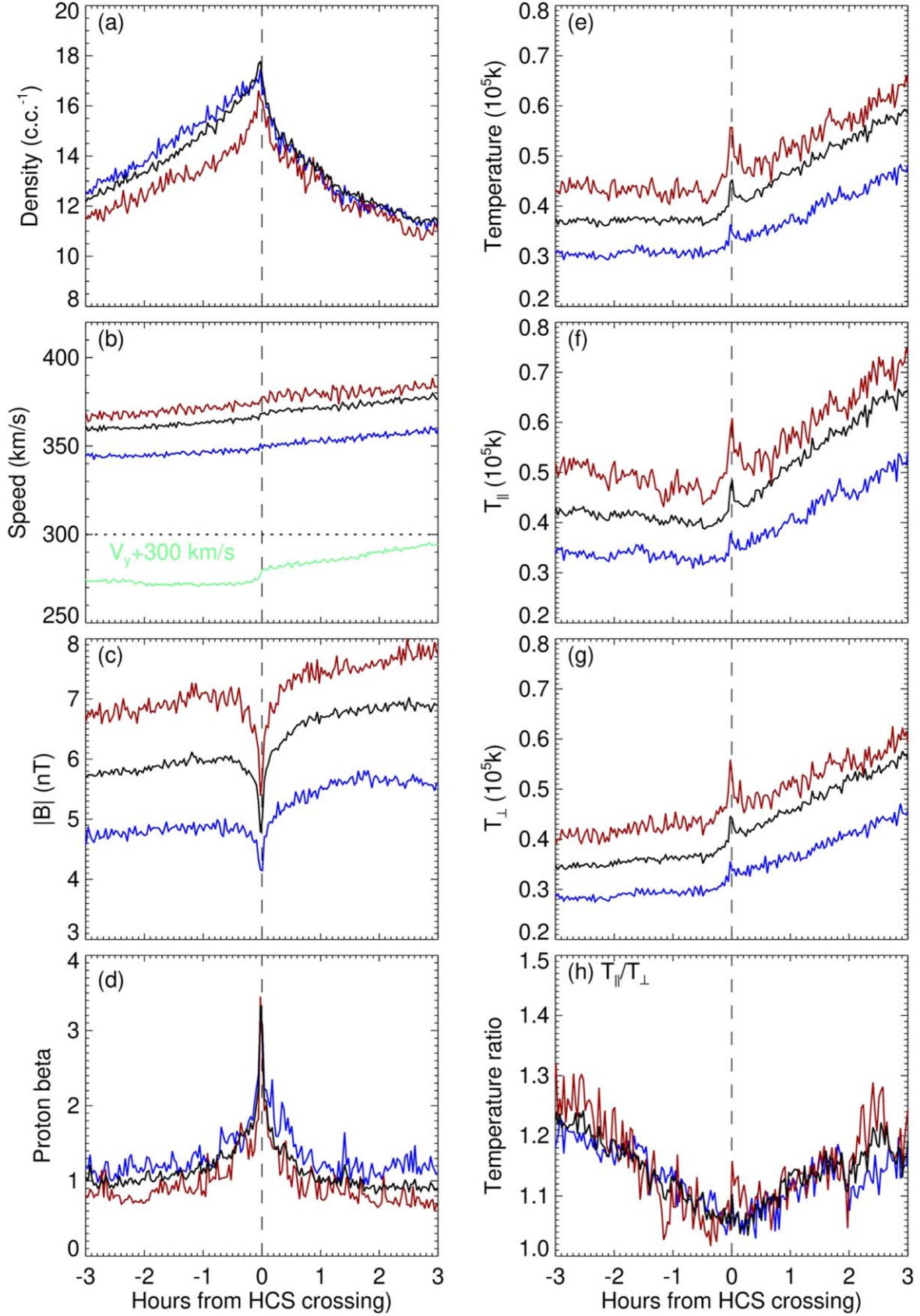


Figure 6. Superposed epoch analysis of the 5 minute averaged solar wind properties in the vicinity (± 6 hr) of the HCS. (a) the proton density, (b) proton speed, (c) magnetic field intensity, (d) proton beta, (e) proton temperature, (f) proton parallel temperature, (g) proton perpendicular temperature, and (h) proton parallel-to-perpendicular temperature. The blue (red) traces are based on solar minimum (maximum) years data (see the text for details).

clearly discernible, the gross properties of the plasma in the vicinity of the current sheets and at the current sheets are similar.

The current sheet is also characterized by a modest ($\sim 10\%$) increase in the proton temperature. The increase is slightly larger in the solar maximum than solar minimum years (see Figure 6(e)). The size of the rising temperature area is smaller than the size of the magnetic field depression, meaning that bulk plasma heating can occur within regions of current sheets. Figures 6(f) and (g) show parallel and perpendicular (relative to the ambient magnetic field) proton temperature. It can be seen that proton heating occurs in both the parallel and perpendicular directions and with a slightly dominant parallel heating (Figure 6(h)). As shown in Figure 5(h), proton temperature anisotropy (T_{\parallel}/T_{\perp}) prevails and is greater than unity in the entire time window and approaches unity (~ 1.05) near the HCS. Surprisingly, this decrease in the temperature ratio does not depend on the solar cycle. The decrease in the proton temperature anisotropy is associated with a mild decrease in the perpendicular temperature and a mild increase in the perpendicular temperature ahead of the current sheet and a steeper increase in the parallel than in the perpendicular temperature behind the current sheet. This suggests that some thermal isotropization processes can take effect when approaching the current sheet. Analysis of the Helios data also suggested that fairly isotropic proton distribution only occurred very close to the sector boundary (Marsch et al. 1982b). In the HCS the temperature anisotropy increased slightly (a few percent), with the most pronounced ($\sim 10\%$) increase during the solar maximum years.

As shown in Figures 5(c) and (h), the HCS resides in the region of large-scale decreasing proton temperature and temperature anisotropy. The presence of the HCS creates a further decrease in the temperature anisotropy. Therefore, this is a unique feature associated with the HCS. The width of the temperature anisotropy dip surrounding the HCS is estimated to be ~ 4 hr (or $\sim 5 \times 10^6$ km) and is much greater than the magnetic field depression region (~ 1 hr) and the temperature enhancement region (~ 20 minutes).

3. Discussion and Summary

In this study we have identified 1197 HCS events associated with the sector boundary using solar wind plasma and field data acquired from the Wind spacecraft in the years 1995–2020, which span two solar cycles or a complete solar magnetic cycle. The current sheet events were fitted by the 1D Harris current model to extract current sheet parameters. A summary of the major findings from our statistical analysis of the current sheet events and discussions are given as follows:

(1) The width of the current sheets at 1 au shows large variability, ranging between ~ 600 km and 1.1×10^6 km with an average width of $1.06(\pm 0.04) \times 10^5$ km and a median width of 5.9×10^4 km. In addition, the current sheet occurrence (N) of certain current sheet width (w in 10^4 km) can be expressed as $\ln(N) = 4.91 - 0.09 w$.

Previous studies have suggested a wide range thickness for the HCS. For example, Winterhalter et al. (1994) analyzed 19 HCS crossings of the HCS by the International Sun-Earth Explorer spacecraft in 1978 and 1979 and found the current sheets' width ranges from $\sim 3 \times 10^3$ to 10^4 km. Using the Wind data acquired during the first 5 months of the mission, Lepping et al. (1996) identified 212 HCS crossings and reported an

average HCS thickness of $\sim 6 \times 10^4$ km. More recently, Blanco et al. (2008) surveyed the Wind data from 1995–2001, which covers the ascending phase of solar cycle 23. Based on a total of 165 events they identified, the width of the HCS is found to be much wider, $9 \pm 5 \times 10^5$ km. Therefore, our numbers generally fall within these reported results.

The present finding that the width of the HCS occurrence follows an exponential distribution. It implies that very wide HCS events are possible but rare, and the majority of the HCS events have widths much less than the simple arithmetic mean. After normalization, the probability function (P) can be expressed as $\ln(P) = 2.16 - 0.09w$ where P and w have units of percentage and 10^4 km, respectively. For a spacecraft near the Earth's orbit, the probability of observing a 1×10^4 km wide HCS is 7.9% and the probability decreases by about a half (to 3.5%) for observing a 1×10^5 km wide HCS.

(2) The longitude of the current sheet normal ranges between 90° and 270° , with a major peak at $\sim 210^\circ (\pm 1^\circ)$ and a minor peak at $\sim 130^\circ$. The mean, standard deviation, and median values of the longitude are $201^\circ (\pm 1^\circ)$, 32° , and 208° , respectively. No solar cycle dependence was found.

The present result is consistent with the work of Blanco et al. (2008), who show an average longitude of $205^\circ (\pm 2^\circ)$ from the Wind data in 1995–2000. However, using the first 5 months of the Wind measurements, Lepping et al. (1996) show, in contrast to our result, a wide spread of the HCS longitude (135° – 315°) without a preferred orientation. Although not explicitly mentioned in their study, we suspect that at least some of their HCS events are not associated with the true large-scale current sheets (e.g., sector boundary) but some small-scale ones generated locally. This is suggested by the much larger rate of occurrence in their current sheet events (212 events in 5 months data or 55 current sheet crossings per solar rotation) than the typical 2–4 sector boundary crossings per solar rotation.

The two-peak ($\sim 210^\circ$ and $\sim 130^\circ$) distribution in the current sheet longitude found in the present study suggests that current sheets at 1 au statistically lie in two preferred orientations. The large peak is close to the predicted Parker spiral field and the minor peak is close to the ortho-Parker spiral field. Figure 3 confirms that the HCS lies along the ambient IMF direction.

(3) The latitude of the HCS normal is also widely spread within $\pm 90^\circ$ with a weak peak around -15° . The average, standard deviation, and median latitude values are $\sim 0^\circ (\pm 1^\circ)$, 43° , and -2° , respectively. No solar cycle dependence is found for the current sheet properties studied.

The warped HCS is due to the offset of the magnetic field dipole axis from the solar rotation axis and subsequent interaction with the solar wind outflow (see Owens & Forsyth 2013, and references therein). When rotating with the Sun, the warped current sheet provides a nonzero attach angle for a spacecraft and produces a sinusoidal variation that changes with the latitude. It has been shown that the amplitude of the sinusoidal variations is smaller near the solar minimum and larger near the solar maximum (Svalgaard & Wilcox 1976). Theoretical consideration even predicts a nearly vertical HCS during the solar maximum (e.g., Hoeksema 1992). Such a predicted variation is not observed here. In contrast, we observed a wide spread in the HCS inclination. The work of Lepping et al. (1996) also shows a wide spread in the inclination of the current sheets observed in 1995 (near the solar minimum). Blanco et al. (2008) studied ~ 7 yr (1995–2001) of HCS events with the Wind data and did not find

the predicted solar cycle variation, although they concluded that more data are needed to reveal the solar cycle variation. It is possible that the wavy nature of the HCS (Villante et al. 1979) may have caused the wide spread in the inclination reported here.

(4) The yearly occurrence rate is relatively constant (~ 46 or 3.4 events per solar rotation), without showing a clear solar cycle dependence.

This is probably not unexpected because typically 2–4 sectors are observed at heliographic low-latitude orbits (e.g., Behannon et al. 1989). A warped HCS (or sector boundary) is expected to increase the chance of an encounter with a spacecraft at high latitudes. For a spacecraft at low latitudes (within $\sim \pm 7.2^\circ$) such as Wind, the HCS warp amplitude is probably larger than Wind’s latitudes, even during solar quiet times, and will be observed anyway. Also, it is generally believed that the sector boundary is formed as a plasma from a coronal hole interacts with plasma from another coronal hole with opposite magnetic field polarities. Observations have suggested multiple current sheets can exist within the sector boundary (Crooker et al. 1993). Furthermore, some theoretical models envision the current sheet can have small-scale waves or ripples (Jokipii & Thomas 1981). Multiple crossings can exist due either to waves or ripples on the single surface or single crossing of multiple current sheets (Neugebauer 2008). Since multiple crossing of small-scale current sheet crossings are ignored in the present study, our result represents the occurrence rate of the sector boundary or the large-scale current sheet crossing.

(5) There are clear solar cycle variations in the properties of the plasma and field within the current sheets and these variations closely follow their background counterparts (except the proton density).

This result strongly suggests that the properties of the HCS are controlled to a certain extent by its background conditions and support the general view that the HCS is a passive structure driven by its ambient solar wind. It is worth mentioning that while the proton density exhibits solar cycle variations, it does not follow the background solar wind density ($r = 0.33$). Typical plasma density associated with the HPS/HCS is around $10\text{--}20\text{ cm}^{-3}$ (e.g., Winterhalter et al. 1994), a few times the background value. Although there are large ($> 50\text{ cm}^{-3}$) density HCS events associated with IP shocks (Liou & Wu 2020), they are probably rare and do not affect the yearly background solar wind density.

(6) A modest ($\sim 10\%$) increase in the solar wind proton temperature at the current sheet relative to its ambient plasma is identified, along with a region of a decrease in the proton temperature anisotropy (T_{\parallel}/T_{\perp}) toward unity when approaching the current sheet from both sides.

The relatively larger proton temperature found in the current sheet than its ambient plasma is one of the key findings of the present analysis. It may suggest a larger heating of the proton and perhaps other species at its base in the corona before escaping from the Sun or some local heating in its way out. Heating of the solar wind proton has been observed (e.g., Marsch et al. 1982b; Schwartz & Marsch 1983). These studies found a higher proton temperature than what adiabatic cooling (Chew et al. 1956) would predict and concluded that additional heating should occur in the solar wind. What the heating sources and where the heating takes place are still not known. It has been suggested that solar wind discontinuities, including the current sheets, can be the site of plasma heating (e.g., Burlaga & Ness 1968; Leamon et al. 2000;

Vasquez & Hollweg 2001; Dmitruk et al. 2004). Indeed, Petschek-type reconnection exhausts have been observed frequently in the solar wind at 1 au (e.g., Gosling et al. 2005a; Davis et al. 2006; Phan et al. 2006, 2009) and beyond (Gosling et al. 2006). Although reconnection exhausts have also been observed at the HCS, they are still relatively rare (Gosling et al. 2005b, 2006; Gosling 2010) and most of the reconnection exhausts have been observed in conjunction with coronal mass ejections (Phan et al. 2009). While enhanced proton density, temperature, temperature anisotropy, proton beta, and reduced magnetic field strength are typical features of the reconnection exhausts (e.g., Gosling et al. 2005a) similar to those observed at the HCS, an enhanced plasma flow is unique to reconnection exhausts and is not observed at the HCS. In addition, the statistical analysis of strong current sheets by Borovsky & Denton (2011) suggests no evidence of solar wind heating. Therefore, reconnection may not be the source of the proton temperature increase at the HCS. More detailed analysis of the plasma parameters at the HCS is necessary to determine the source of proton heating. This is beyond the scope of the present study and will be conducted in a future study.

It is worth discussing the gross feature of proton temperature anisotropy (T_{\parallel}/T_{\perp}) near the HCS. Proton temperature anisotropy is expected in the expanding solar wind as a result of weak collisional plasma undergoing adiabatic cooling (e.g., Chew et al. 1956). This has been confirmed by measurements in the solar wind from 0.3–1 au (Marsch et al. 1982b). A decrease in the proton temperature anisotropy from greater than unity to nearly unity has also been observed in the solar wind a couple of days before and after the sector boundary by these researchers. It is important to point out that while the present study is consistent with Marsch et al.’s (1982b) general finding in the gross feature of temperature anisotropy surrounding the HCS, we also identified a relatively small region of large proton anisotropy depression just a few hours before and after the HCS crossings. This region is wider than the width of density enhancements and magnetic field depression region as indicated in Figure 6. This finding indicates that close to the HCS some unknown processes are at work to reduce the anisotropy. Coulomb collisions may play an important role in isotropization due to very low temperature and very high density at the HCS and its surroundings (Marsch et al. 1982a). On the other hand, temperature anisotropy can excite kinetic instabilities in the solar wind, which in turn reduces the temperature anisotropy (e.g., Hellinger et al. 2006; Matteini et al. 2007). Matteini et al. (2013) studied the stability of the current sheet using numerical hybrid simulations and suggested that in the presence of proton anisotropy with $T_{\parallel}/T_{\perp} > 1$ in the background, firehose fluctuations can be excited. Wave-particle interactions will reduce the proton anisotropy toward unity and stabilize the HCS.

Finally, at the HCS, a modest ($\sim 10\%$ during solar maximum and smaller during solar minimum) increase in the proton temperature anisotropy is also observed. This feature has not been reported previously. Together with the modest ($\sim 10\%$) proton temperature increase at the HCS, it suggests mild heating of the proton exists with slightly preferential parallel heating. On the other hand, it is also possible that some intermittent sources of heating such as reconnection and intermittent turbulence are at work (e.g., Osman et al. 2014). Observations have shown that the proton temperature can increase significantly (approximately a few times) within a reconnection exhaust (see, e.g., Figure 2 of

Gosling et al. 2005a). The small temperature increase may be an averaging effect.

4. Conclusions

We have studied 1197 HCS/SB crossing events using plasma and field observations from Wind during the years 1995–2020 to explore the gross characteristic properties of the HCS/SB in the low latitude of the heliosphere at 1 au over the entire solar magnetic cycle. Statistical examinations of these HCS events have revealed some new general properties of the HCS in addition to confirm some well-known features established previously. Lack of a solar cycle dependence in the HCS general configuration (e.g., occurrence, inclination, etc.) is, among others, surprising. Evidence in proton heating within the HCS is identified. We also show evidence that the heating is not isotropic and the preferential heating leads to isotropization of proton toward the HCS. Further studies are required to understand such a property.

The solar wind plasma (SWE), IMF (MFI), and super-thermal electron (3DP) data were provided by the Goddard Space Flight Center/Space Physics Data Facility (<ftp://spdf.gsfc.nasa.gov/pub/data/wind>). The work of C.-C.W. was partially supported by the Chief of Naval Research and by NASA grants 80HQTR19T0062, 80HQTR18T0023, and 80HQTR20T0067 to the Naval Research Laboratory. This study was also supported by NRL grant N00173-20-1-G005 to the Johns Hopkins University Applied Physics Laboratory.

References

- Behannon, K. W., Burlaga, L. F., Hoeksema, J. T., et al. 1989, *JGR*, **94**, 1245
- Blanco, J. J., Rodríguez-Pacheco, J., Hidalgo, M. A., et al. 2008, *JASTP*, **70**, 226
- Blanco, J. J., Rodríguez-Pacheco, J., & Sequeiros, J. 2003, *SP*, 213, 147
- Borovsky, J. E. 2010, *JGR*, **115**, A09101
- Borovsky, J. E., & Denton, M. H. 2011, *ApJL*, **739**, L61
- Borini, G., Gosling, J. T., Bame, S. J., et al. 1981, *JGR*, **86**, 4565
- Burlaga, L. F., & Ness, N. F. 1968, *CaJPS*, **46**, 962
- Burlaga, L. F., Ness, N. F., & Acuña, M. H. 2007, *ApJ*, **668**, 1246
- Burton, M. E., Crooker, N. U., Siscoe, G. L., et al. 1994, *JGR*, **99**, 1
- Chew, G. F., Goldberger, M. L., & Low, F. E. 1956, *RSPSA*, **236**, 112
- Crooker, N. U., Huang, C.-L., Lamassa, S. M., et al. 2004, *JGR*, **109**, A03107
- Crooker, N. U., Siscoe, G. L., Shodhan, S., et al. 1993, *JGR*, **98**, 9371
- Davis, M. S., Phan, T. D., Gosling, J. T., et al. 2006, *GeoRL*, **33**, L19102
- Dmitruk, P., Matthaeus, W. H., & Seenu, N. 2004, *ApJ*, **617**, 667
- Feldman, W. C., Asbridge, J. R., Bame, S. J., et al. 1973, *JGR*, **78**, 6451
- Gosling, J. T. 2007, *ApJL*, **671**, L73
- Gosling, J. T. 2010, in AIP Conference Proc. 1216, 12th Int. Solar Wind Conf. (Melville, NY: AIP), 188
- Gosling, J. T., Asbridge, J. R., Bame, S. J., et al. 1978, *JGR*, **83**, 1401
- Gosling, J. T., Eriksson, S., Skoug, R. M., et al. 2006, *ApJ*, **644**, 613
- Gosling, J. T., & Pizzo, V. J. 1999, in Corotating Interaction Regions, ed. A. Balogh et al. (Berlin: Springer), 21
- Gosling, J. T., Skoug, R. M., McComas, D. J., et al. 2005a, *JGR*, **110**, A01107
- Gosling, J. T., Skoug, R. M., McComas, D. J., et al. 2005b, *GeoRL*, **32**, L05105
- Harris, E. G. 1962, *Nuovo Cim*, **23**, 115
- Hellinger, P., Trávníček, P., Kasper, J. C., et al. 2006, *GeoRL*, **33**, L09101
- Hoeksema, J. T. 1992, in Solar Wind Seven, Proc. 3rd COSPAR Coll., Vol. 3, ed. E. Marsch & R. Schwenn (New York: Pergamon), 191
- Hoeksema, J. T., Wilcox, J. M., & Scherrer, P. H. 1983, *JGR*, **88**, 9910
- Huang, J., Liu, Y. C.-M., Klecker, B., et al. 2016, *JGRA*, **121**, 19
- Hundhausen, A. J. 1977, in Coronal Holes and High Speed Wind Streams, ed. J. B. Zirker (Boulder, CO: Colorado Associated. Univ. Press), 225
- Hundhausen, A. J., Bame, S. J., Asbridge, J. R., et al. 1970, *JGR*, **75**, 4643
- Jokipii, J. R., & Thomas, B. T. 1981, *ApJ*, **243**, 1115
- Kahler, S. W., & Lin, R. P. 1994, *GeoRL*, **21**, 1575
- Kahler, S. W., & Lin, R. P. 1995, *SP*, 161, 183
- Lavraud, B., Fargette, N., Réville, V., et al. 2020, *ApJL*, **894**, L19
- Leamon, R. J., Matthaeus, W. H., Smith, C. W., et al. 2000, *ApJ*, **537**, 1054
- Lee, M. A. 2000, *JGR*, **105**, 10491
- Lepping, R. P., Acuna, M., Burlaga, L., et al. 1995, *SSRv*, **71**, 207
- Lepping, R. P., Szabo, A., Peredo, M., et al. 1996, *GeoRL*, **23**, 1199
- Lin, R. P., Anderson, K. A., Ashford, S., et al. 1995, *SSRv*, **71**, 125
- Liou, K., & Wu, C.-C. 2016, *SP*, 291, 3777
- Liou, K., & Wu, C.-C. 2020, *JPhCS*, **1620**, 012011
- Liu, Y. C.-M., Huang, J., Wang, C., et al. 2014, *JGRA*, **119**, 8721
- Marsch, E., Mühlhäuser, K.-H., Rosenbauer, H., et al. 1982a, *JGR*, **87**, 35
- Marsch, E., Mühlhäuser, K.-H., Schwenn, R., et al. 1982b, *JGR*, **87**, 52
- Matteini, L., Hellinger, P., Goldstein, B. E., et al. 2013, *JGRA*, **118**, 2771
- Matteini, L., Landi, S., Hellinger, P., et al. 2007, *GeoRL*, **34**, L20105
- Ness, F., & Wilcox, J. M. 1964, *PRL*, **13**, 461
- Neugebauer, M. 2008, *JGR*, **113**, A12106
- Ogilvie, K. W., Chorney, D. J., Fitzenreiter, R. J., et al. 1995, *SSRv*, **71**, 55
- Osman, K. T., Matthaeus, W. H., Gosling, J. T., et al. 2014, *PhRvL*, **112**, 215002
- Owens, M. J., & Forsyth, R. J. 2013, *LRSP*, **10**, 11
- Phan, T. D., Gosling, J. T., Davis, M. S., et al. 2006, *Natur*, **439**, 175
- Phan, T. D., Gosling, J. T., & Davis, M. S. 2009, *GeoRL*, **36**, L09108
- Pizzo, V. J. 1991, *JGR*, **96**, 5405
- Richardson, J. D., Stone, E. C., Cummings, A. C., et al. 2006, *GeoRL*, **33**, L21112
- Riley, P., Linker, J. A., & Mikić, Z. 2002, *JGR*, **107**, 1136
- Schulz, M. 1973, *Ap&SS*, **24**, 371
- Schwartz, S. J., & Marsch, E. 1983, *JGR*, **88**, 9919
- Schwenn, R. 1990, in Physics of the Inner Heliosphere I, ed. R. Schwenn & E. Marsch (Berlin: Springer), 99
- Siscoe, G. L. 1972, *JGR*, **77**, 27
- Smith, E. J. 1993, in The Sun in Time, ed. C. P. Sonett, M. S. Giampapa, & M. S. Mathews (Tucson, AZ: Univ. of Arizona Press)
- Smith, E. J. 2001, *JGR*, **106**, 15819
- Smith, E. J., & Wolfe, J. H. 1976, *GeoRL*, **3**, 137
- Suess, S. T., Ko, Y.-K., von Steiger, R., et al. 2009, *JGR*, **114**, A04103
- Svalgaard, L., & Wilcox, J. M. 1976, *Natur*, **262**, 766
- Szabo, A., Larson, D., Whittlesey, P., et al. 2020, *ApJSS*, **246**, 47
- Vasquez, B. J., & Hollweg, J. V. 2001, *JGR*, **106**, 5661
- Villante, U., Bruno, R., Mariani, F., Burlaga, L., et al. 1979, *JGR*, **84**, 6641
- Wilcox, J. M., Hoeksema, J. T., & Scherrer, P. H. 1980, *Sci*, **209**, 603
- Wilcox, J. M., & Ness, N. F. 1965, *JGR*, **70**, 5793
- Winterhalter, D., Smith, E. J., Burton, M. E., et al. 1994, *JGR*, **99**, 6667
- Wu, C.-C., Liou, K., & Lepping, R. P. 2019, *SP*, 294, 90
- Wu, C.-C., Liou, K., Wu, S. T., et al. 2016, in AIP Conference Proc. 1720, Solar Wind 14 (Melville, NY: AIP), 040021
- Yin, Z., Zou, H., Ye, Y., et al. 2019, *SW*, **17**, 1756
- Zhou, X.-Y., Smith, E. J., Winterhalter, D., et al. 2005, in Proc. Solar Wind 11—SOHO 16, Connecting Sun and Heliosphere ESA SP-592, ed. B. Fleck et al. (Paris: ESA)